



Excitation-energy dependence of fission-fragment neutron multiplicity in the improved scission-point model

H. Paşca 

*Joint Institute for Nuclear Research, 141980 Dubna, Russia
and “Babeş-Bolyai” University, Faculty of Physics, 400084 Cluj-Napoca, Romania*

A. V. Andreev and G. G. Adamian 

Joint Institute for Nuclear Research, 141980 Dubna, Russia

N. V. Antonenko

*Joint Institute for Nuclear Research, 141980 Dubna, Russia
and Tomsk Polytechnic University, 634050 Tomsk, Russia*



(Received 6 October 2023; accepted 12 March 2024; published 1 April 2024)

For the neutron-induced fission of nuclei $^{235,238}\text{U}$, the evolution of the shape of fission-fragment neutron multiplicity distribution with increasing excitation energy is explored within the improved scission-point model. For a wide range of incident neutron energies, the dependence of an average number of neutrons emitted per a fission event on the excitation energy is studied.

DOI: [10.1103/PhysRevC.109.044601](https://doi.org/10.1103/PhysRevC.109.044601)

I. INTRODUCTION

The improved scission-point model is able to consistently and reliably describe several fission observables simultaneously [1–14] in the case of electromagnetically induced fission of the Th and U isotopes. The main ingredient of this model is the calculation of the potential energy surface (PES) since its characteristics control all the fission observables. Owing to the common PES, mass/charge distributions, fission-fragment total kinetic energy (TKE), and neutron multiplicity are correlated. One of the most interesting questions regarding the binary decay of a nucleus is the role of shell effects in the process. As found for the fission of the Th and U isotopes [11–14], the symmetric mass/charge distributions are the result of the liquid-drop-like behavior of the system, while the asymmetric peaks in the aforementioned distributions originate from strong microscopic shell correction energies. As the excitation energy of the fissioning system increases, the shell effects are expected to melt away, leaving the system with the liquid-drop behavior characterized by symmetric mass/charge fragmentation and large fragment deformation values. As a result of these changes in the PES, the mass/charge yields, TKE, and neutron multiplicities are expected to be affected. For example, highly deformed fragments lead to low TKE values but also enhance the neutron multiplicity, as the deformation energy is restored to fission-fragments after separation as an internal excitation energy.

The present work focuses on the influence of excitation energy on the mass distribution, TKE value, and the neutron multiplicity in highly excited fissioning $^{236,239}\text{U}$ isotopes. Focusing on several observables for which there are a lot of experimental data, one can draw a better picture of how the transition from the PES ruled by a microscopic shell correction energy to the PES dominated a macroscopic energy affects the fission outcome. The establishment of correlations

between the fission characteristics seems to be useful for analyzing the experimental data. Note the present work is the natural continuation of our previous paper [14], where the improved scission-point model was employed.

II. MODEL

The most important step of the scission-point model [1–14] is the calculation of the potential energy of the dinuclear system (DNS) as a function of charge Z_i , mass A_i , deformations β_i (the ratios between the major and minor semiaxes of the fragments) of two fragments, and the internuclear distance R between them [8,9,11–14]. The index i designates a light (L) or (H) heavy fragment. The scission configuration is represented as two axially deformed and uniformly charged ellipsoids—the nascent fragments. The two nuclei are fully formed and possess all the features of isolated nuclei, e.g., binding energies, according to the separability principle, and mutually interact through the nuclear and Coulomb forces. Their orientation is frozen to a tip-to-tip configuration that provides the minimum interaction energy. Owing to the repulsive nature of the Coulomb interaction V^C and attractive nature of the nuclear interaction V^N , a potential pocket is formed in R coordinate with a minimum at $R = R_m$, which roughly corresponds to a separation of $d = 0.5\text{--}1$ fm between the tips of the fragments [4], depending on the mass $A_{L,H}$ and charge $Z_{L,H}$ numbers, and deformations $\beta_{L,H}$. The depth B_{qf} of the potential pocket ensures that the DNS is in local equilibrium over all collective coordinates before the decay. Since the model assumes statistical equilibrium at the scission point, one can reduce the complexity of the problem by fixing the internuclear distance $R = R_m$ at the bottom of the potential pocket. Then, the potential energy

$$U = U_L^{\text{LD}} + \delta U_L^{\text{shell}} + U_H^{\text{LD}} + \delta U_H^{\text{shell}} + V^C + V^N \quad (1)$$

of the system is calculated as the sum of the energies of the fragments (the LD energy U_i^{LD} plus shell-correction energy $\delta U_i^{\text{shell}}$) and the energy $V^{\text{int}} = V^C + V^N$ of the fragment-fragment interaction [14]. The shell corrections are calculated with the Strutinsky method for an axially deformed nucleus [15]. The interaction potential consists of the Coulomb interaction potential V^C of two uniformly charged ellipsoids and the nuclear interaction potential V^N taken in the double-folding form [16,17]. Since the excitation energies of the fragments at the scission point are relatively large, we have neglected the pairing energy in the calculations. The interplay between the LD surface energy, the nucleus-nucleus interaction potential, and the shell-correction energy is one of main reasons for the appearance or disappearance of an asymmetric minimum in the potential energy surface. As shown in Ref. [18], the macroscopic effects play an important role in asymmetric fission at low and high excitation energies.

The relative formation and decay probability of the DNS with particular masses, charges, and deformations of the fragments is calculated within the statistical approach as follows [14]:

$$w(A_i, Z_i, \beta_i, \tilde{E}^*) = N_0 \exp \left[-\frac{U(A_i, Z_i, \beta_i, R_m) + B_{qf}(A_i, Z_i, \beta_i)}{T} \right], \quad (2)$$

where N_0 is the normalization factor. In Eq. (2), the temperature is calculated as $T = \sqrt{\tilde{E}^*/a}$ where $a = A/12 \text{ MeV}^{-1}$ is the level density parameter. We use a single temperature T corresponding to the excitation energy \tilde{E}^* of the DNS or compound nucleus (CN) with the lowest potential energy. This temperature corresponds to the global minimum on the PES. The excitation energy of the DNS with primary fragments (Z_i, A_i) is $E^*(A_i, Z_i, \beta_i) = E_{\text{CN}}^* + [U_{\text{CN}}(A, Z, \beta) - U(A_i, Z_i, \beta_i, R_m)]$, where U_{CN} and E_{CN}^* are the binding (potential) and excitation energies of the CN, respectively. In order to obtain the relative yield $Y(Z_i, A_i)$ of a particular primary fragment with mass number A_i and atomic number Z_i , one should integrate Eq. (2) over β_L and β_H . In order to simulate the minimal experimental uncertainties, the mass yields $Y(A_i)$ are smoothed using the Gaussian function with the width $\sigma = 0.5 \text{ u}$. The charge yields $Y(Z_i)$ are not smoothed. A smoothing procedure with larger σ will hide the energy difference of different mass fragmentations effectively averaging them [11]. Since we are interested in all observables, and each observable is strongly affected by the PES, we think it is illustrative to highlight such differences in the energy of different configurations, so a larger σ value is unwarranted. Note that the main reason behind adding such a smearing function is to take effectively into account the experimental conditions.

Supposing that all nucleus-nucleus interaction energy transforms after fission into the $\text{TKE}(A_i, Z_i, \beta_i) = V^C(A_i, Z_i, \beta_i, R_b) + V^N(A_i, Z_i, \beta_i, R_b)$ of the DNS primary fragments with (A_i, Z_i) , we calculate the mean value of the TKE as a function of A_i by averaging over the deformations $\beta_{L,H}$ of the primary fragments and summing over Z_i .

Since at scission the deformations of fragments are larger than those in their ground states, the fragments are relaxed to the ground states after the DNS decays and the energies $U_{L,H}^{\text{def}}$ of deformations are transformed into the fragment intrinsic excitation energies. In order to calculate the probability for a

given neutron multiplicity ν per a fission event,

$$P(\nu) = \sum_{Z_i, A_i} \int d\beta_L d\beta_H P_\nu(A_i, Z_i, \beta_i, E^*) \times w(A_i, Z_i, \beta_i, \tilde{E}^*),$$

$$P_\nu(A_i, Z_i, \beta_i, E^*) = \sum_{\nu_L=0}^{\nu} \int_0^{E^*} d\epsilon_L^* P_C(\epsilon_L^*) P_{\nu_L}(U_L^{\text{def}} + \epsilon_L^*) \times P_{\nu-\nu_L}(E^* + U_H^{\text{def}} - \epsilon_L^*), \quad (3)$$

we should take into account the fluctuation of the excitation energy between light and heavy pre-scission fragments using the microcanonical distribution $P_C(\epsilon_i^*) \sim \rho_i(\epsilon_i^*) \rho_{\bar{i}}(E^* - \epsilon_i^*)$ (where if $i = L(H)$ then $\bar{i} = H(L)$) and ρ_i are the Fermi-gas level densities $\rho_i(\epsilon_i^*) \sim \exp[2(a_i \epsilon_i^*)^{1/2}]$ without any back shift in fragments $i = L, H$ of energy partitioned between two fragments of the DNS and the Jackson formula [14,19]

$$P_{\nu_i}(\epsilon_i) = P'(\nu_i) - P'(\nu_i + 1),$$

$$P'(\nu_i) = 1 - e^{-\Delta_{\nu_i}} \left[\sum_{k=0}^{2\nu_i-3} \frac{(\Delta_{\nu_i})^k}{k!} \right], \quad (4)$$

for the probability of evaporation of exactly ν_i neutrons from the excited post-scission fragment i with excitation energy $\epsilon_i = \epsilon_i^* + U_i^{\text{def}}$. In Eq. (4), $\Delta_{\nu_i} = (\epsilon_i - \sum_{k=1}^{\nu_i} B_k^{(i)})/T_i$, where $B_k^{(i)}$ is the experimental neutron binding energy at the k th evaporation step and $T_i = (12\epsilon_i/A_i)^{1/2}$ is the temperature. Here the quantities $P'(\nu_i)$ and $P'(\nu_i + 1)$ are the probabilities of emission of at least ν_i and $\nu_i + 1$ neutrons, respectively. Since $P'(\nu_i = 1) = 1$ at $\epsilon_i > B_1^{(i)}$, then $P_{\nu_i=1} = 1$ at $B_1^{(i)} < \epsilon_i \leq B_1^{(i)} + B_2^{(i)}$ and $P_{\nu_i=1} = e^{-\Delta_2} [1 + \Delta_2]$ at $\epsilon_i > B_1^{(i)} + B_2^{(i)}$. Note that our model simply does not treat gamma emission.

Analogously, one can calculate the average neutron multiplicities from two fission fragments [14],

$$\langle \nu \rangle(Z_i) = \sum_{A_i, \nu} \int d\beta_L d\beta_H \nu P_\nu(A_i, Z_i, \beta_i, E^*) w(A_i, Z_i, \beta_i, \tilde{E}^*),$$

$$\langle \nu \rangle(A_i) = \sum_{Z_i, \nu} \int d\beta_L d\beta_H \nu P_\nu(A_i, Z_i, \beta_i, E^*) w(A_i, Z_i, \beta_i, \tilde{E}^*), \quad (5)$$

and the neutron multiplicities from one fission fragment,

$$\langle \nu_i \rangle(Z_i) = \sum_{A_i, \nu_i} \int d\beta_L d\beta_H \nu_i \tilde{P}_{\nu_i}(A_i, Z_i, \beta_i, E^*) \times w(A_i, Z_i, \beta_i, \tilde{E}^*),$$

$$\langle \nu_i \rangle(A_i) = \sum_{Z_i, \nu_i} \int d\beta_L d\beta_H \nu_i \tilde{P}_{\nu_i}(A_i, Z_i, \beta_i, E^*) \times w(A_i, Z_i, \beta_i, \tilde{E}^*),$$

$$\tilde{P}_{\nu_i}(A_i, Z_i, \beta_i, E^*) = \int_0^{E^*} d\epsilon_i^* P_C(\epsilon_i^*) P_{\nu_i}(U_i^{\text{def}} + \epsilon_i^*). \quad (6)$$

The main ingredient of our description within the improved scission-point fission model [14] is the sophisticated potential energy as a function of mass (charge) asymmetry, deformations of nuclei, and internuclear distance. The refinement of

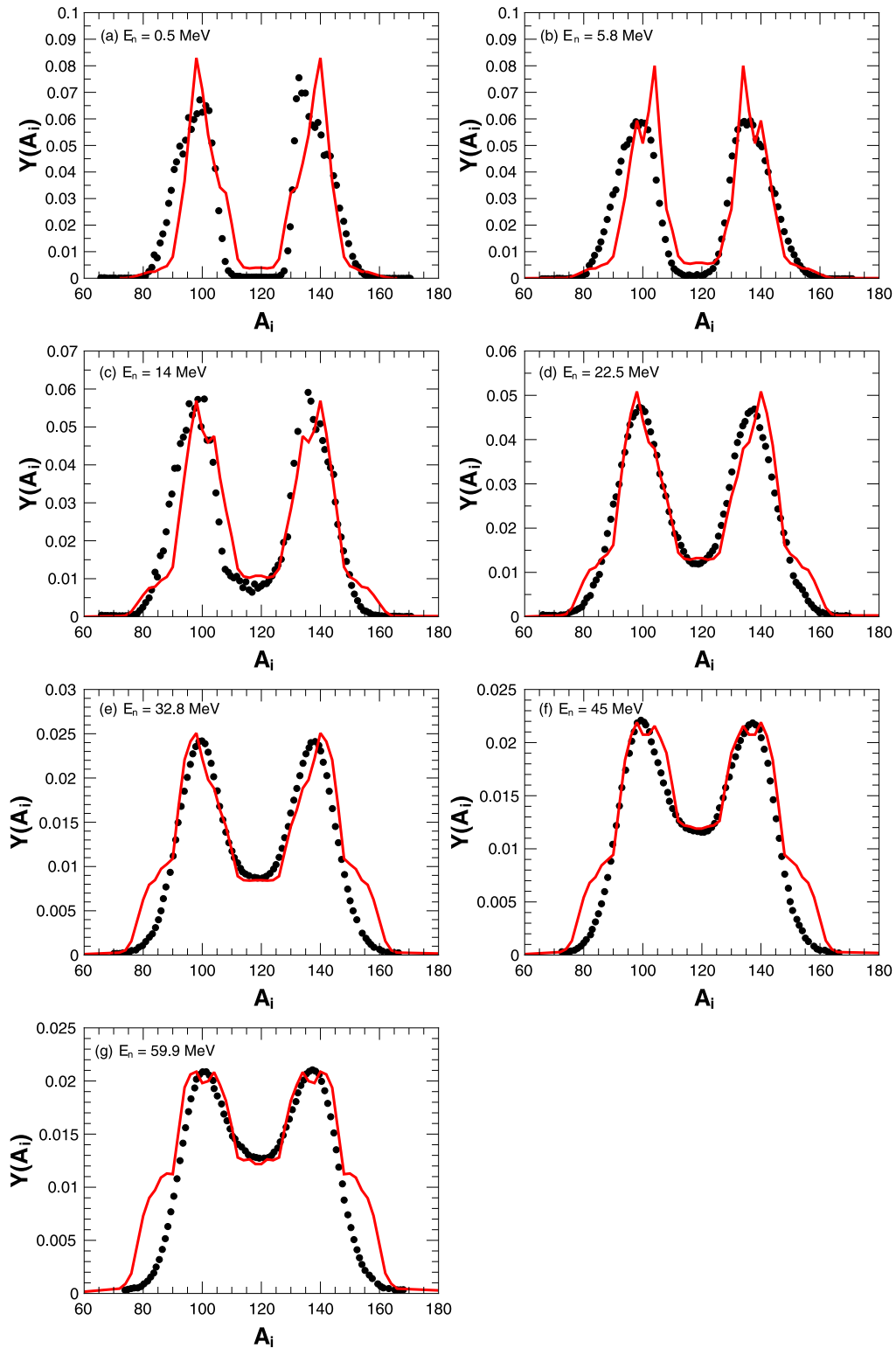


FIG. 1. The mass distribution of the fission fragments originating from the neutron-induced fission of ^{238}U as a function of the mass number of one of the fragments. The solid lines represent theoretical results and the symbols are experimental data [23,24] and [25] at the incident neutron energies $E_n = 0.5, 5.8, 14, 22.5$ and $32.8, 45, 59.9$ MeV, respectively.

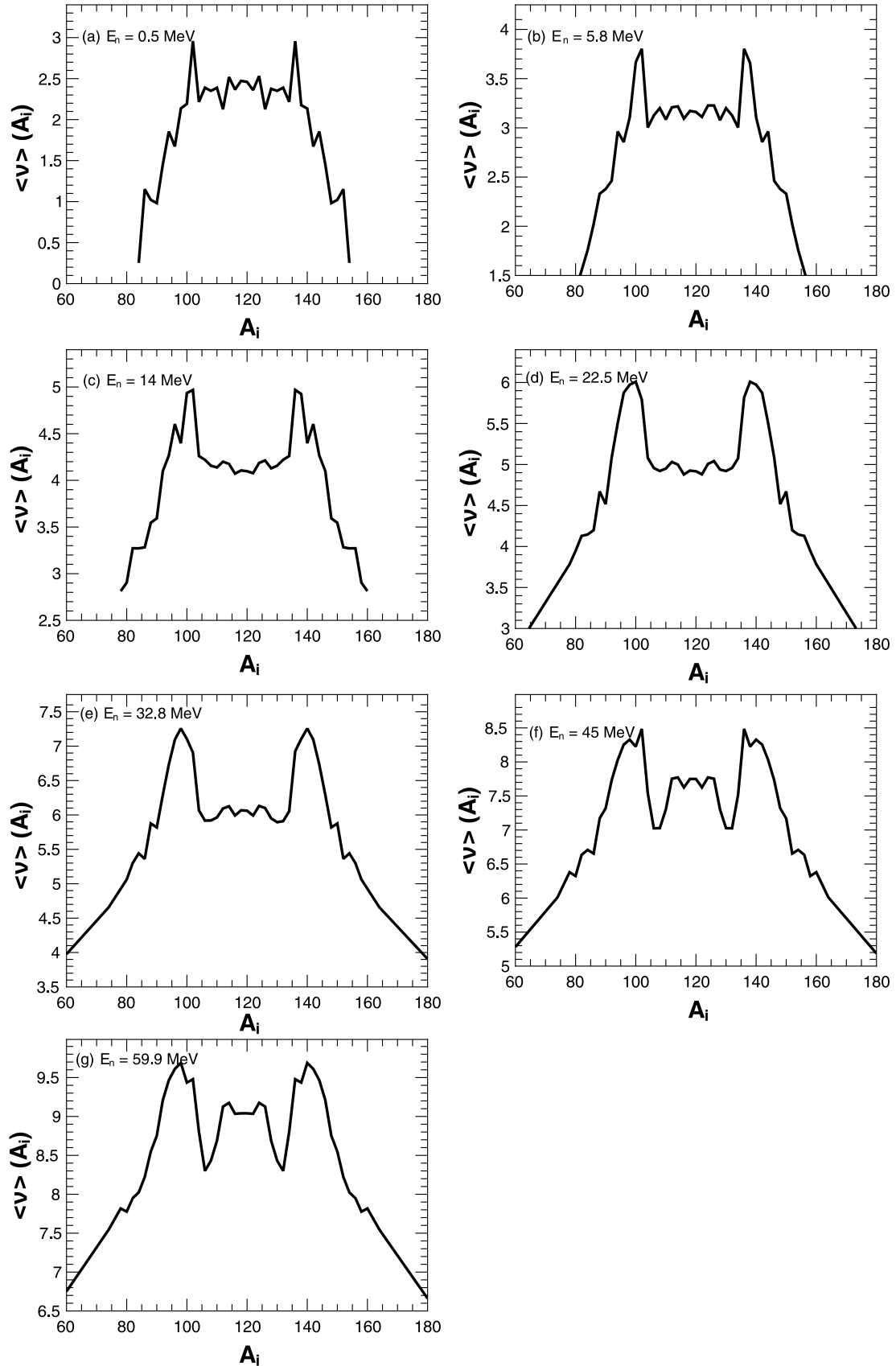


FIG. 2. The average neutron multiplicity distribution $\langle \nu \rangle(A_i)$ as a function of the mass number of one of the fragments resulting from the $^{238}\text{U}(n, f)$ reaction. The incident neutron energy E_n is indicated in each panels.

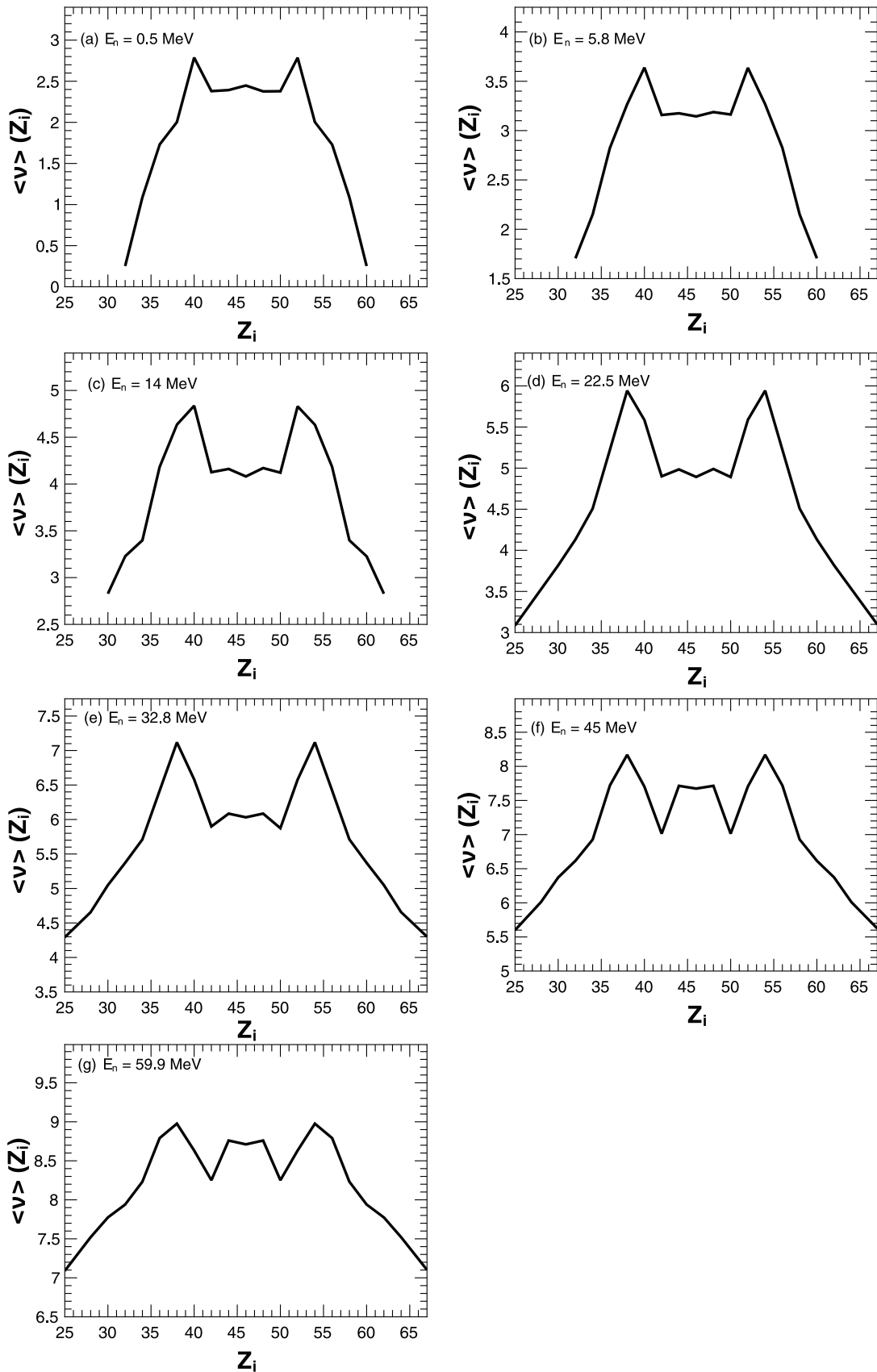


FIG. 3. The average neutron multiplicity distribution $\langle \nu \rangle(Z_i)$ as a function of the charge number of one of the fragments resulting from the $^{238}\text{U}(n, f)$ reaction. The incident neutron energy is indicated in each panels.

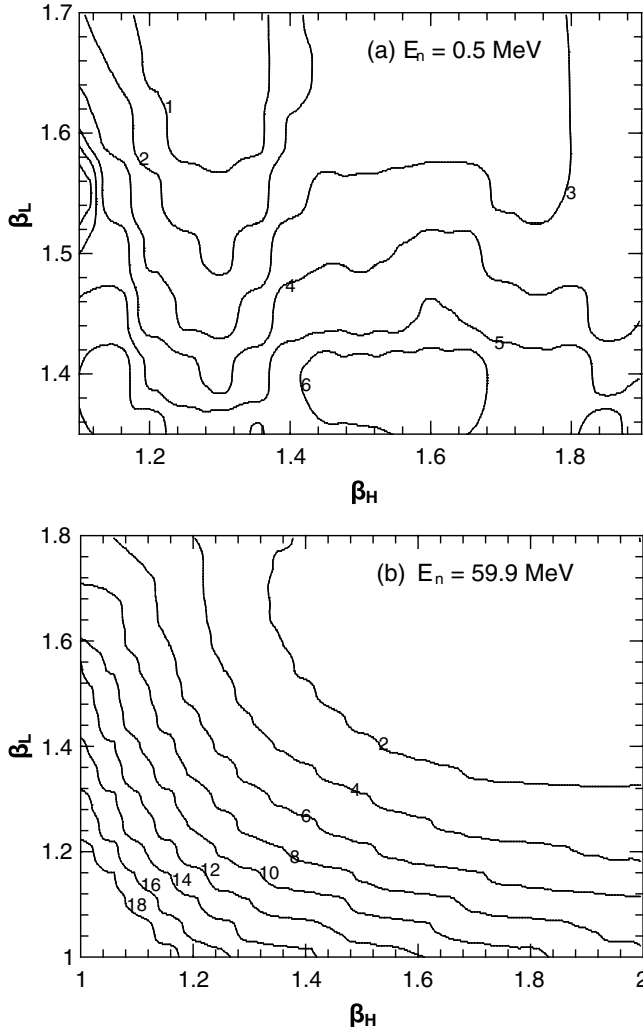


FIG. 4. The PES corresponding to the $^{99}\text{Sr} + ^{140}\text{Te}$ fragmentation of ^{239}U . The incident neutron energies are (a) $E_n = 0.5$ MeV and (b) $E_n = 59.9$ MeV.

the scission-point model is the introduction of temperature- and isospin-dependent liquid-drop energy, which allowed us to describe and explain the mass/charge distributions resulting from spontaneous and induced fission. The knowledge of deformations of the nascent DNS fragments is crucial at the moment of scission. Our model differs from the scission-point model of Ref. [1] by a better definition of the scission configuration and the excitation energy. For each point on the PES, one can accurately calculate the excitation energy (as the difference between the total energy of the CN and the energy of the system at the scission point), and hence the temperature. The distance between the tips of the fission fragments at scission and excitation energy are defined from the nucleus-nucleus interaction potential and PES.

Within the improved scission-point model we describe the yields for fission of U isotopes without employing the multichance fission assumption. The fission at first chance seems to be the most important and the contribution of multichance fission does not change the shape of the mass, charge, and neutron multiplicity distributions [20]. This is supported by

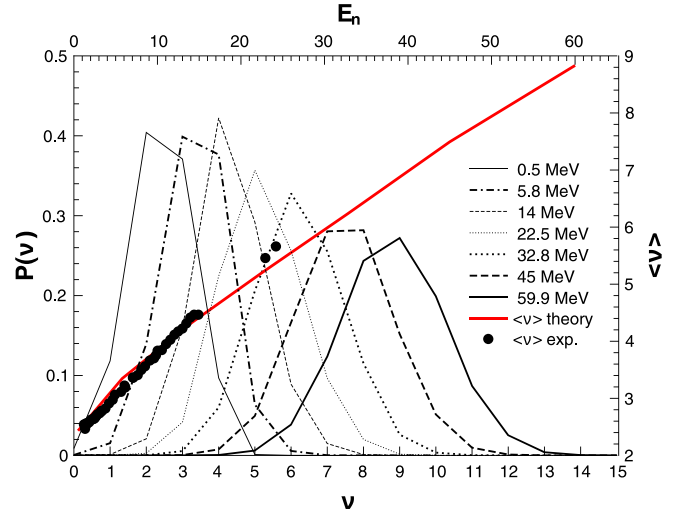


FIG. 5. The calculated probabilities $P(\nu)$ (lines) as functions of the neutron multiplicity ν and the calculated average number of neutrons $\langle \nu \rangle$ (thick red line) emitted per a fission event in the case of the $^{238}\text{U}(n, f)$ reaction at the indicated neutron energies E_n . The symbols represent the experimental [28,29] results for the $\langle \nu \rangle$ at different E_n .

the experimental data [21] in which the number of pre-scission neutrons does not exceed 2 at excitation energies about 50 MeV of Th and U isotopes. The largest differences between calculated and experimental neutron multiplicities, less than 1 u, appear for actinides.

III. CALCULATED RESULTS AND DISCUSSION

As seen from Eq. (2), the probability of finding the DNS in a specific configuration depends strongly on the charge and mass asymmetry of the system, as well as on the deformations of two fragments. Keeping the deformations constant and tracing the potential energy in the charge/mass coordinate, one usually finds that $U(A_i, Z_i)$ exhibits a single minimum at $A_i \simeq A_{\text{CN}}/2$, $Z_i \simeq Z_{\text{CN}}/2$ for fissioning preactinides and two minima for fissioning actinides. If the system is also allowed to evolve in the deformation plane (β_L , β_H), then for each possible fragmentation $(Z_L, A_L) + (Z_H, A_H)$ one or several minima are also observed. These minima are the result of the complex interplay between the macroscopic binding energies of the fragments, the fragment-fragment interaction potential, and the microscopic shell correction energies in the fragments [11–14,22]. If the minima are formed mainly due to the interaction and macroscopic LD energies, the fragments are of relatively equal mass and charge and tend to have large deformations. On the other hand, if the fragments are the result of strong microscopic shell energies, they tend to be formed with mass and charge numbers, which differ strongly from $A_{\text{CN}}/2$ or $Z_{\text{CN}}/2$, and to have large stiffness, and usually the deformation parameters are small.

The origin of the minima in the PES plays a significant role in establishing where the minima are located in the (β_L , β_H) plane, which, in turn, influences the TKE of the fragments and neutron multiplicity. If the minima are due to strong mi-

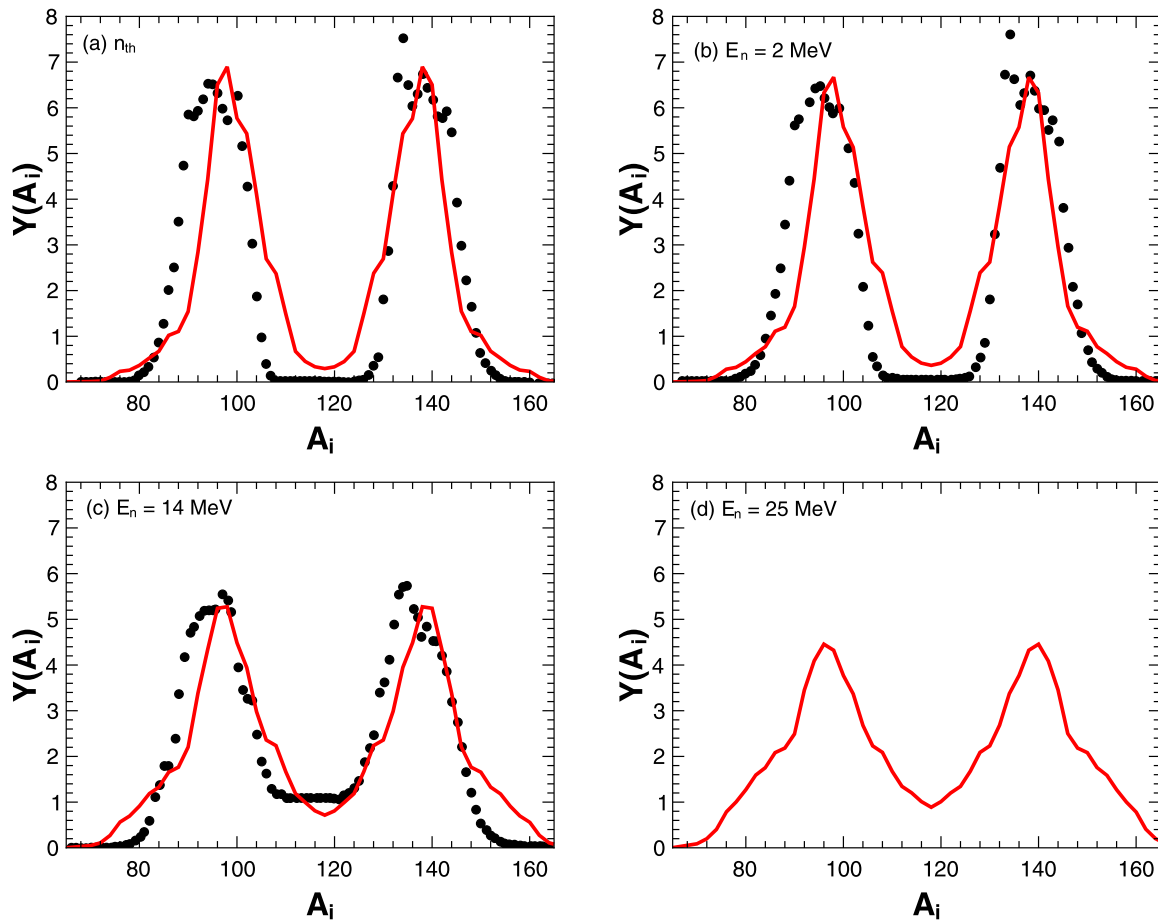


FIG. 6. The same as in Fig. 1 but for the $^{235}\text{U}(n, f)$ reaction at the indicated neutron energies.

crossopic effects, then small deformations lead to large TKE values. Conversely, if the macroscopic energies dominate, then TKE values will be lower.

Furthermore, different values of the deformation parameters lead to different deformation energies of the light and heavy fragments at scission. These energies are recovered postsission as internal excitation energies of two separated fragments. Additional intrinsic excitation energy plays a major role in neutron emission [14], so the overall location of the minima in the (β_L, β_H) plane and their origin determine and correlate with TKE values and neutron multiplicities ν .

In Fig. 1, the experimental (symbols) [23–25] and calculated (lines) mass distributions of the fission fragments resulting from the neutron-induced fission of ^{238}U are presented at various neutron energies. The location of the maxima and average widths of these distributions are well reproduced. Note that in Fig. 1 the measured data represent the secondary fission-fragment distribution, while the theoretical values refer to the primary distribution.

For the lowest neutron energies [Figs. 1(a), 1(b)], the mass distributions exhibit two asymmetric maxima separated by a deep minimum at symmetry. With increasing neutron energy (and consequently excitation energy) the symmetric component of the distribution increases. We note that even at $E_n = 59.9$ MeV the asymmetric character of the distribution is still clear, with a peak-to-valley ratio of about 1.5.

Thus, the transition from asymmetric to symmetric yields in the first-chance fission occurs at high excitation energies, $E^* > 65$ MeV. However, we note that to describe the yields of fission of actinides at high excitation energies with the dynamical models of Refs. [26,27] and the phenomenological model of Ref. [28], one should take the multichance fission into account. In these models, the transition from asymmetric to symmetric mass/charge yields is obtained in the first-chance fission at relatively low excitation energy, $E^* \approx 20$ MeV [26,27]. Thus, the asymmetric component of the mass (charge) distribution is mainly attributed to the late-chance fission. The main difference between these models [26,27] and the improved scission-point model arises from the difference of their PES at scission point.

The average neutron multiplicities $\langle \nu \rangle$ from both fission fragments are presented in Fig. 2 as a function of mass number A_i for the $^{238}\text{U}(n, f)$ reaction at the indicated neutron energies. Note that for the fission of actinides U and Pu our model also describes well the average neutron multiplicities from one fission fragment as a function of fragment mass number A_i [14]. In Fig. 3, the $\langle \nu \rangle$ is presented as a function of the charge number Z_i of one of the fragments, for the same reaction and neutron energies as in Fig. 2. For $E_n = 0.5$ MeV and 5.8 MeV [Figs. 2(a), 2(b) and 3(a), 3(b)], the neutron multiplicity exhibits a rather weak dependence on the mass (charge) numbers in the range $A_i = 100$ –140 ($Z_i = 38$ –54), with the

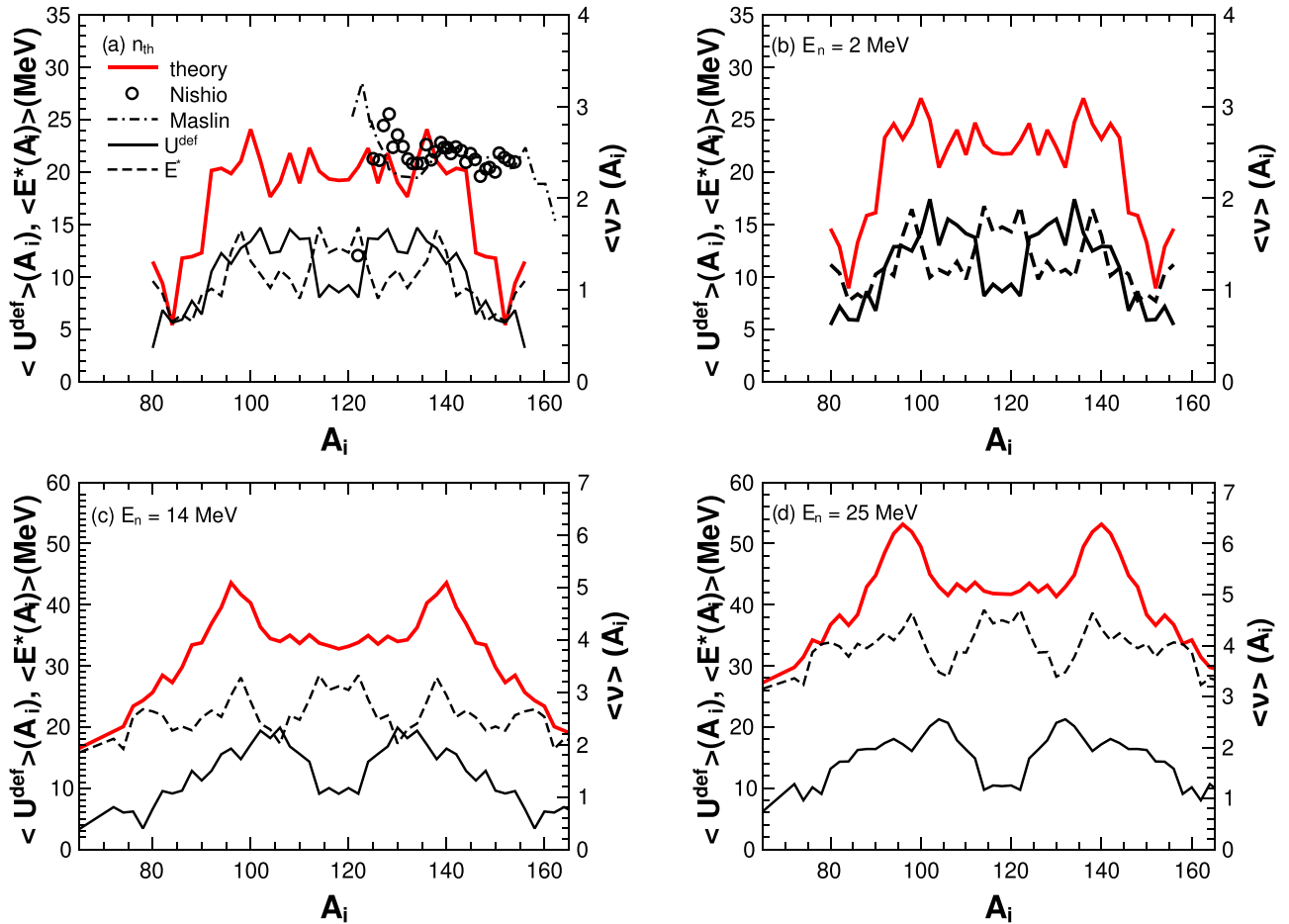


FIG. 7. The calculated (red solid lines) and experimental (the dash-dotted line [30] and symbols [31]) average neutron multiplicity distributions $\langle \nu \rangle(A_i)$ (the right axis) as a function of the mass number of one of the fragments resulting from the $^{235}\text{U}(n, f)$ reaction. The incident neutron energy E_n is indicated in each panel. The calculated deformation $\langle U^{def} \rangle(A_i)$ (solid lines) and excitation $\langle E^* \rangle(A_i)$ (dashed lines) energies of fission fragments at scission (the left axis).

exception of noticeable maxima at $A_L = 98$ ($Z_L = 38$) and $A_H = 138$ ($Z_H = 54$). These maxima are easy to explain: at ^{98}Sr there is a minimum in U and correspondingly a maximum in the mass/charge distribution. Therefore, this scission configuration also exhibits the highest excitation energy, which promotes the neutron emission. The plateau in the neutron multiplicity formed at symmetry is due to the liquid-drop-like behavior of the PES, which presents large deformations (and deformation energies) that compensate for a relatively low DNS excitation energy.

As the incident neutron energy increases, the symmetric mass yields in Fig. 1 also increase. As the shell correction energies decrease, the system is governed more and more by the interplay between the macroscopic LD and the interaction energy. Thus, the minima in the (β_L, β_H) plane migrate to higher deformations, and become more shallow and widen. To illustrate this, we present in Fig. 4 the PES of $^{99}\text{Sr} + ^{140}\text{Te}$ at two different incident neutron energies, $E_n = 0.5$ and 59.9 MeV, respectively. The values of U are normalized so that U corresponding to the PES minimum has a value equal to zero, for convenience.

As ^{140}Te is rather close to the proton $Z = 50$ shell closure, it exhibits a large stiffness so that the optimum deformation for this nucleus is rather small at low energies. Its complement, however, is a soft nucleus with optimum deformation far from its ground-state value [see Fig. 4(a)]. As the excitation energy increases, the shell correction energy is diminished and the total potential energy is dominated by the macroscopic LD and interaction energies. As a result, the ^{140}Te nucleus also acquires a large deformation, and the minimum in the PES widens. With increasing excitation energy and deformation energy and the fact that more configurations are available at large energies than at low energy, the asymmetric peaks in the $\langle \nu \rangle$ distributions of Figs. 2 and 3 become more pronounced. Also, with increasing excitation energy, the symmetric fragments also evaporate more neutrons, so the overall number of neutrons emitted per a fission event increases.

At very large excitation energies the minima in the PES reach their final shape so that the asymmetric maxima in the mass distributions start to saturate [Figs. 1(f), 1(g)], while the symmetric component still increases with excitation energy. Similarly, with increasing excitation energy the asymmetric

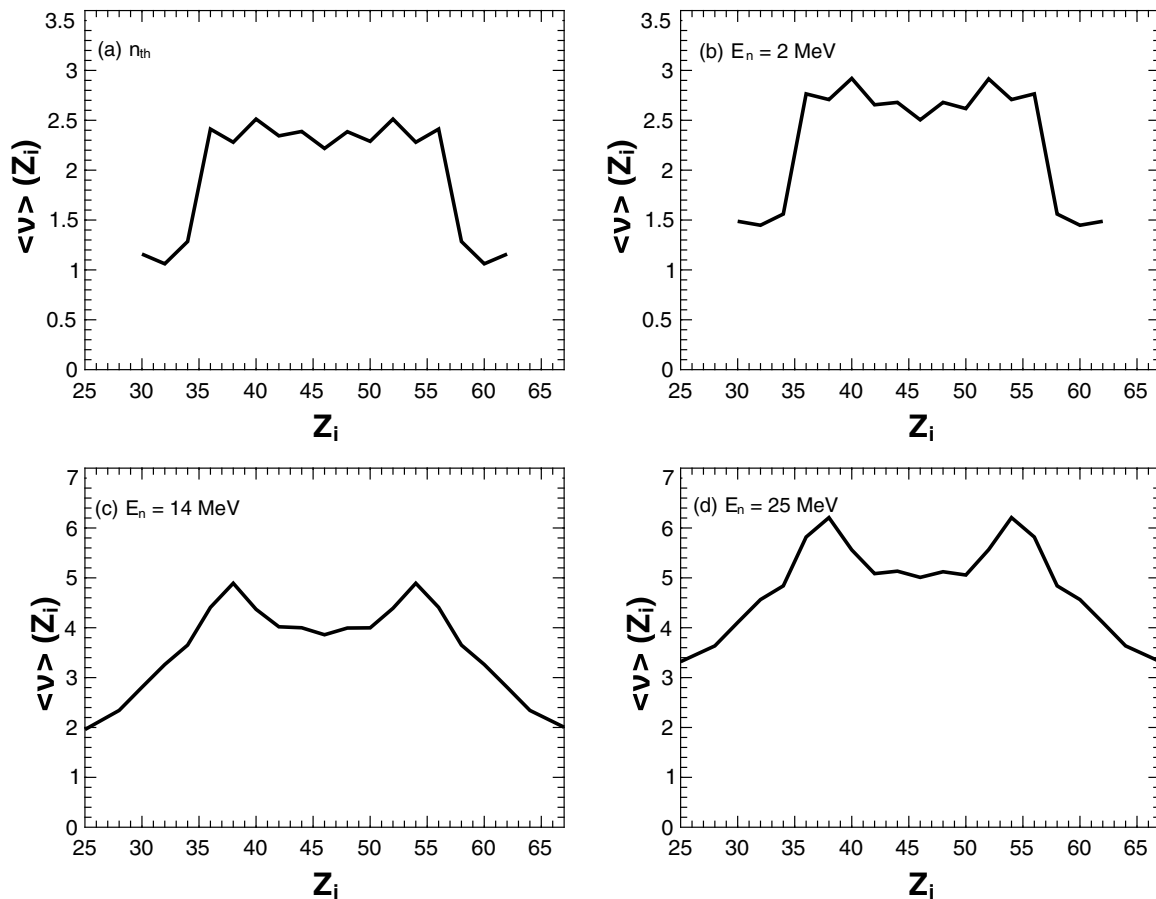


FIG. 8. The same as in Fig. 3 but for the $^{235}\text{U}(n, f)$ reaction at the indicated neutron energies.

peaks in the $\langle \nu \rangle(A_i)$ and $\langle \nu \rangle(Z_i)$ distributions [Figs. 2(f), 2(g) and 3(f), 3(g)] are fully formed at the largest excitation energies. The symmetric part of these distributions starts exhibiting maxima due to an increase in the excitation energy of symmetric fragmentations.

In Fig. 5, the average number of neutrons $\langle \nu \rangle$ emitted per a fission event is compared with the experimental data [28,29]. The agreement between the theoretical results and the measured values is excellent up to $E_n = 14$ MeV, and the deviation between them at $E_n = 22$ –25 MeV is about 0.3 units. In both theory and experiments, $\langle \nu \rangle(E_n)$ changes slope with increasing energy, which can be explained by the stabilization of the PES minima with increasing excitation energy as discussed above. At the highest excitation energies, an increase in $\langle \nu \rangle$ is simply due to an increase in excitation energies, while at low and intermediate excitation energies an increase in deformation energy is also responsible.

In Fig. 5, we also present the probabilities $P(\nu)$ of the system to emit exactly ν neutrons for the indicated energies. As expected, the maximum of the probabilities shifts with increasing energy to larger values of ν . The probability distributions also widen with increasing excitation energy as more configurations become energetically available.

In Fig. 6, we show the theoretical (solid lines) and experimental (symbols) [23,24] fission-fragment mass distribution resulting from the $^{235}\text{U}(n, f)$ reaction at thermal neutron en-

ergy [Fig. 6(a)], $E_n = 2$ MeV [Fig. 6(b)], 14 MeV [Fig. 6(c)], and 25 MeV [Fig. 6(d)], respectively. The agreement between the measured and theoretical values is rather good, and the explanation for the changes in the mass yield shape is the same as in the $^{238}\text{U}(n, f)$ case. Figures 7 and 8 present the predicted

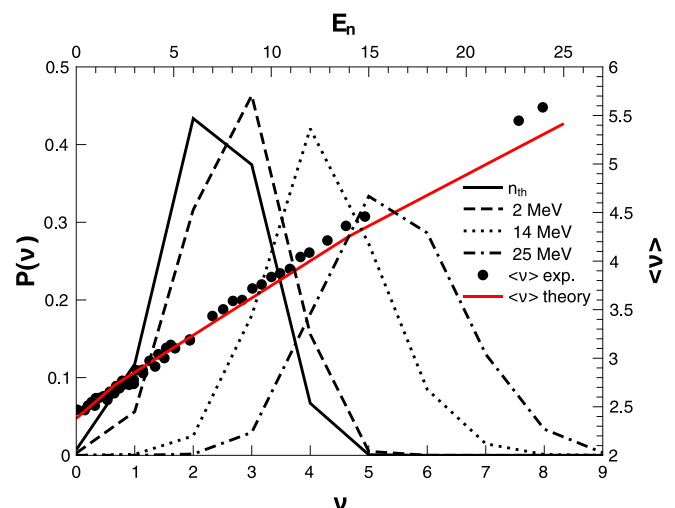


FIG. 9. The same as in Fig. 5 but for the $^{235}\text{U}(n, f)$ reaction at the indicated neutron energies.

neutron multiplicities as a function of mass and charge numbers, respectively, of one of the fragments. As can be seen in Fig. 7, the calculations of $\langle \nu \rangle(A_i)$ for the thermal neutron-induced fission are in quite satisfactory agreement with the experimental data [30,31]. As in the case of $^{238}\text{U}(n, f)$ reaction, at the lowest energies $\langle \nu \rangle(A_i)$ [Figs. 7(a), 7(b)] and $\langle \nu \rangle(Z_i)$ [Figs. 8(a), 8(b)] have a very weak dependence on the mass/charge asymmetry. At $E_n = 14$ and 25 MeV, the formation of asymmetric peaks in the multiplicity distributions is observed. The explanation for them is the same as in the $^{238}\text{U}(n, f)$ case.

As seen in Fig. 7, for the $^{235}\text{U}(n, f)$ reaction, the intrinsic excitation energy $\langle E^* \rangle(A_i)$ of both fragments at scission is high around the symmetry and the deformation energy $\langle U^{\text{def}} \rangle(A_i)$ of both fragments at scission is small in this mass region even at the lowest excitation energy of the CN. At $E_n = E_{n_h}$, 2 MeV and $A_L \approx 100\text{--}112$, $\langle U^{\text{def}} \rangle > \langle E^* \rangle$. In the asymmetric region, $\langle U^{\text{def}} \rangle < \langle E^* \rangle$ at $E_n = 14$ and 25 MeV. After scission (after the transform of the deformation energy to the intrinsic excitation energy) the total excitation energy of both fragments is rather constant with some fluctuations in the region $A_L \approx 100\text{--}118$, and it is reflected in the rather constant value for the neutron multiplicity.

In Fig. 9, the experimental and theoretical average number of neutrons $\langle \nu \rangle$ emitted per a fission event is shown as a function of incident neutron energy for the $^{235}\text{U}(n, f)$ reaction. Again, the measured values [28,29] are well reproduced, with a slight underestimation, about 0.3 units, in the $E_n = 20\text{--}25$ MeV range. Again, we note the change of the slope of $\langle \nu \rangle$ with increasing E_n , which reflects the stabilization of the PES minima with increasing excitation energy.

To verify the fact that the PES minimum stabilizes at some final (β_L, β_H) values as the microscopic shell correction energy diminishes with increasing E_n , the experimental average total kinetic energy $\langle \text{TKE} \rangle$ (symbols) of fission fragments [32] is compared with the theoretical results (solid line) for the $^{235}\text{U}(n, f)$ reaction at different values of E_n (Fig. 10). In both experiment and theory $\langle \text{TKE} \rangle$ decreases by a few MeV in the range $E_n = 0\text{--}25$ MeV, and then it reaches a saturation value at $E_n > 35$ MeV. Since $\langle \text{TKE} \rangle$ is strongly influenced by the (β_L, β_H) values, this saturation strongly indicates that the PES minima migrate to a final (β_L, β_H) value and then they stabilize there. We note that the calculated $\langle \text{TKE} \rangle$ values in Fig. 10 overestimate the experimental values by about 7 MeV. The same procedure used here was used by us in Ref. [14] for the calculation of $\langle \text{TKE} \rangle(Z_i)$ values of fission fragments resulting from the γ -ray-induced fission of $^{222,226,230}\text{Th}$ ($E_\gamma = 11$) MeV. In Ref. [14], there was excellent agreement between theoretical and measured total kinetic energies. Also, the experimental [33] $\langle \text{TKE} \rangle$ values for fissioning ^{234}U ($E_\gamma = 11$ MeV) are $\langle \text{TKE} \rangle = 171.9 \pm 3.4$ MeV, while for fissioning ^{226}Th ($E_\gamma = 11$ MeV), $\langle \text{TKE} \rangle = 167.7 \pm 3.3$ MeV and for fissioning $^{239}\text{Pu}(n, f)$ ($E_n = 0.5$ MeV), $\langle \text{TKE} \rangle = 181.3$ MeV. The calculated $\langle \text{TKE} \rangle$ values seem to agree well with the measured values for fissioning ^{234}U ($E_\gamma = 11$ MeV) and they are in between the values obtained in fission of the Th and Pu isotopes. The calculated values of $\langle \text{TKE} \rangle$ in Fig. 10 are

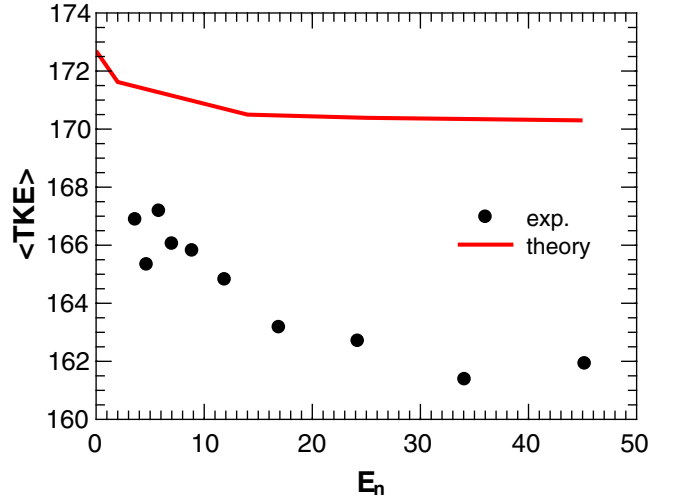


FIG. 10. The average total kinetic energy $\langle \text{TKE} \rangle$ of the fission fragments as a function of incident neutron energy for the $^{235}\text{U}(n, f)$ reaction. The solid line represents the theoretical results, while the symbols are the experimental data of Ref. [32].

close to those obtained for ^{234}U ($E_\gamma = 11$ MeV). The difference between theory and experiment in Fig. 10 deserves further theoretical and experimental study. However, even though there is an overestimation of the absolute value of the fission-fragment total kinetic energy, the energy trend is well reproduced.

IV. CONCLUSIONS

For the neutron-induced fission of $^{235,238}\text{U}$ at different incident neutron energies, the experimental mass distributions have been well described with the improved scission-point model. The average neutron multiplicity $\langle \nu \rangle$ as a function of mass/charge of one of the fragments is predicted to exhibit a weak dependence on Z_i (A_i) for low excitation energies, while at intermediate excitation energies ($E^* = 20\text{--}40$ MeV) a two-peaked distribution is expected. At the highest excitation energies studied here, a more complex three-peaked distribution is predicted. Simultaneously, the average number $\langle \nu \rangle$ of neutrons emitted per a fission event is also shown to agree very well with the measured data for a large range of incident neutron energies. As shown, the $\langle \nu \rangle$ increases almost linearly with E_n , which can be explained by the combined effect of an increase in excitation energy accompanied by an increase in deformation energy associated with diminishing microscopic shell correction energies especially for magic (double magic) nuclei. At high E_n , stabilization of the minima in the PES at large values of (β_L, β_H) is predicted to show a slight change in the slope of $\langle \nu \rangle(E_n)$ and saturation of the average fission-fragment total kinetic energy $\langle \text{TKE} \rangle$.

ACKNOWLEDGMENTS

This work was supported by the Ministry of Science and Higher Education of the Russian Federation (Contract No. 075-10-2020-117).

- [1] B. D. Wilkins, E. P. Steinberg, and R. R. Chasman, *Phys. Rev. C* **14**, 1832 (1976).
- [2] T. Matsuse, C. Beck, R. Nouicer, and D. Mahboub, *Phys. Rev. C* **55**, 1380 (1997).
- [3] S. J. Sanders, A. Szanto de Toledo, and C. Beck, *Phys. Rep.* **311**, 487 (1999).
- [4] A. V. Andreev, G. G. Adamian, N. V. Antonenko, S. P. Ivanova, and W. Scheid, *Eur. Phys. J. A* **22**, 51 (2004); A. V. Andreev, G. G. Adamian, N. V. Antonenko, and S. P. Ivanova, *ibid.* **26**, 327 (2005).
- [5] S. Panebianco, J.-L. Sida, H. Goutte, J.-F. Lemaître, N. Dubray, and S. Hilaire, *Phys. Rev. C* **86**, 064601 (2012).
- [6] A. V. Andreev, G. G. Adamian, and N. V. Antonenko, *Phys. Rev. C* **86**, 044315 (2012); A. V. Andreev, G. G. Adamian, N. V. Antonenko, and A. N. Andreyev, *ibid.* **88**, 047604 (2013).
- [7] M. Caamaño *et al.*, *Phys. Rev. C* **92**, 034606 (2015).
- [8] H. Paşca, A. V. Andreev, G. G. Adamian, and N. V. Antonenko, *Phys. Rev. C* **94**, 064614 (2016).
- [9] H. Paşca, A. V. Andreev, G. G. Adamian, and N. V. Antonenko, *Phys. Rev. C* **97**, 034621 (2018); *Nucl. Phys. A* **969**, 226 (2018).
- [10] J.-F. Lemaître, S. Goriely, S. Hilaire, and J.-L. Sida, *Phys. Rev. C* **99**, 034612 (2019).
- [11] H. Paşca, A. V. Andreev, G. G. Adamian, and N. V. Antonenko, *Phys. Rev. C* **101**, 064604 (2020).
- [12] H. Paşca, A. V. Andreev, G. G. Adamian, and N. V. Antonenko, *Phys. Lett. B* **760**, 800 (2016).
- [13] H. Paşca, A. V. Andreev, G. G. Adamian, and N. V. Antonenko, *Phys. Rev. C* **104**, 014604 (2021); Y. H. Zhang, J. J. Li, N. Tang, X. R. Zhang, Z. Liu, and F. S. Zhang, *ibid.* **107**, 024604 (2023).
- [14] H. Paşca, A. V. Andreev, G. G. Adamian, and N. V. Antonenko, *Phys. Rev. C* **108**, 014613 (2023).
- [15] J. Maruhn and W. Greiner, *Z. Phys.* **251**, 431 (1972).
- [16] G. G. Adamian *et al.*, *Int. J. Mod. Phys. E* **05**, 191 (1996).
- [17] G. G. Adamian, N. V. Antonenko, and W. Scheid, in *Clustering Effects within the Dinuclear Model*, Lecture Notes in Physics, edited by Christian Beck (Springer, Berlin, 2012).
- [18] H. Paşca, A. V. Andreev, G. G. Adamian, and N. V. Antonenko, *Int. J. Mod. Phys. E* **32**, 2340005 (2023).
- [19] R. Vandenbosch and J. R. Huizenga, *Nuclei Fission* (Academic, New York, 1973).
- [20] H. Paşca, A. V. Andreev, G. G. Adamian, and N. V. Antonenko, *Eur. Phys. J. A* **54**, 104 (2018).
- [21] D. Hilscher and H. Rossner, *Ann. Phys. (France)* **17**, 471 (1992).
- [22] H. Paşca, A. V. Andreev, G. G. Adamian, and N. V. Antonenko, *Eur. Phys. J. A* **52**, 369 (2016).
- [23] T. R. England and B. F. Rider, Los Alamos National Laboratory Report LA-UR-94-3107, 1994; M. E. Gooden *et al.*, *Nucl. Data Sheets* **131**, 319 (2016); K. Shibata, O. Iwamoto, T. Nakagawa, N. Iwamoto, and A. Ichihara *et al.*, *J. Nucl. Sci. Technol.* **48**, 1 (2011).
- [24] K. H. Schmidt and B. Jurado, *Rep. Prog. Phys.* **81**, 106301 (2018).
- [25] I. V. Ryzhov, S. G. Yavshits, G. A. Tutin, N. V. Kovalev, A. V. Saulski, N. A. Kudryashev, M. S. Onegin, L. A. Vaishnena, Y. A. Gavrikov, O. T. Grudzevich, V. D. Simutkin, S. Pomp, J. Blomgren, M. Osterlund, P. Andersson, R. Bevilacqua, J. P. Meulders, and R. Prieels, *Phys. Rev. C* **83**, 054603 (2011).
- [26] P. Möller and C. Schmitt, *Eur. Phys. J. A* **53**, 7 (2017).
- [27] K. Hirose *et al.*, *Phys. Rev. Lett.* **119**, 222501 (2017).
- [28] K.-H. Schmidt, B. Jurado, C. Amouroux, and C. Schmitt, *Nucl. Data Sheets* **131**, 107 (2016).
- [29] V. V. Malinovskij, V. G. Vorob'eva, and B. D. Kuz'minov, Report INDC(CCP)-239 (IAEA, Vienna, Austria, 1985).
- [30] E. E. Maslin, A. L. Rodgers, and W. G. F. Core, *Phys. Rev.* **164**, 1520 (1967).
- [31] K. Nishio, Y. Nakagome, H. Yamamoto, and I. Kimura, *Nucl. Phys. A* **632**, 540 (1998).
- [32] R. Yanez, L. Yao, J. King, W. Loveland, F. Tovesson, and N. Fotiades, *Phys. Rev. C* **89**, 051604(R) (2014).
- [33] K.-H. Schmidt *et al.*, *Nucl. Phys. A* **665**, 221 (2000); K.-H. Schmidt, J. Benlliure, and A. R. Junghans, *ibid.* **693**, 169 (2001); C. Böckstiegel *et al.*, *ibid.* **802**, 12 (2008).